31st Congress of the International Council of the Aeronautical Sciences

Belo Horizonte, Brazil; September 09-14, 2018

OUTBOARD SPLIT FLAP AERODYNAMICS OF A FLYING WING CONFIGURATION

Stefan Pfnür , Christian Breitsamter

*Technical University of Munich, Department of Mechanical Engineering, Chair of Aerodynamics and Fluid Mechanics, Boltzmannstr. 15, 85748 Garching, Germany

Keywords: *Aerodynamics, Directional Controllability, Flying Wing, Wind Tunnel, CFD*

Abstract

The yaw-control device of a low-aspect-ratio flying-wing configuration is investigated. The novel layout of the so-called outboard split flap with its hinge-line along the swept leading edge is designed to achieve beneficial yaw-control characteristics. Force and moment measurements as well as stereo particle image velocimetry measurements allow for the analysis of the aerodynamics of the control device. Additionally, Unsteady Reynolds-Averaged Navier-Stokes simulations are performed and compared to the experimental data. Different outboard split flap deflections are investigated at zero degree angle of attack and sideslip. The created force and moment increments of the deflected flap show, that the yawing moment is created by a force vector composed of a drag and side force contribution of similar magnitude. The effective lever arm of the outboard flap increases with the flap deflection angle and reaches a value of the magnitude of the wing half span. The wake flow shows significant axial and lateral velocities in consequence of the deflected flap, which can be associated with the forces originating at the flap. The numerical results represent the characteristics of the outboard flap well with minor deviations in the absolute values.

1 Introduction

Flying wings belong to the category of the All-Lifting-Vehicles (ALV). Such configurations do not feature vertical surfaces, but all elements of the aircraft are aerodynamically shaped to contribute to the lift. A significant disadvantage of flying wings is the reduced stability and control [1–4]. The absence of a vertical tail entails a considerable reduction of the directional stability of the configuration. Therefore, the directional stability and controllability must be provided by control devices integrated in the wing. Furthermore, low-aspect-ratio-wing configurations with medium leading-edge sweep exhibit a small wing span, which requires effective yaw-control devices. The strongly changing flow field at the wing throughout the angle-of-attack polar features attached flow at low angles of attack, flow separation with areas of irregular flow and vortical flow at medium to high angles of attack. Consequently, robust control devices with a sufficient control effectiveness at various freestream conditions are required. Several yaw-control concepts for flying wings have been investigated. Publications are available for e.g. all moving wing tips [5], elevons [1], split wing tips [6], blowing [7], or drag rudders [8].

The Chair of Aerodynamics and Fluid Mechanics of the Technical University Munich (TUM-AER) investigates a novel yaw-control device of a low-aspect-ratio flying-wing configuration with medium leading-edge sweep. The so-called outboard split flap (O/F) needs to provide a sufficient yawing moment to ensure the directional stability and control throughout the polar. Previous investigations on the yaw-control efficiency revealed a strong non-linear characteristic

of the O/F [9]. A comparison of numerical results with the experimental data revealed certain disagreements especially for large O/F deflections. In this study, the aerodynamic characteristic of the O/F is investigated in detail. The created force at the O/F, the effective lever arm and the wake flow are discussed. A comparison with the numerical results of the Unsteady Reynolds-Averaged Navier-Stokes (URANS) simulations gives information on the capability of the applied numerical tools to represent the overall characteristics of the O/F and to determine the source of the observed disagreements in the previous investigations.

2 Flying Wing Configuration

2.1 Wing Geometry

The investigated flying wing configuration features a wing planform in a diamond shape with a positive leading-edge sweep of $\varphi_{LE} = 55°$ and a negative trailing-edge sweep of $\varphi_{TE} = -25°$, see Fig. 1. The root and tip chord of the associated wind tunnel model read $c_r = 1.2\,m$ and $c_t = 0.03\,m$, respectively, and the wing span is $b = 1.235\,m$. This results in a wing aspect ratio of $AR = 2.001$ and a taper ratio of $\lambda = 0.025$. The mean aerodynamic chord is $l_\mu = 0.801\,m$ and the aerodynamic moments are given with respect to the moment reference point $x_{mrp} = 0.501\,m$. The flying-wing configuration is equipped with the symmetric NACA64A012 airfoil and exhibits no twist over the wing span. The airfoil leading edge is sharpened within the first 20 percent of the wing semi span. This airfoil modification provokes a flow separation in the apex region already at low angles of attack. Additional information on the airfoil design and the aerodynamic relevance of the leading-edge modification can be found in Refs. [10, 11].

2.2 Outboard Split Flap Geometry

The flying wing is equipped with a so-called outboard split flap (O/F) integrated in the wing tip section, see Fig. 1. The O/F is split with respect to the $z = 0$ plane in an upper and lower

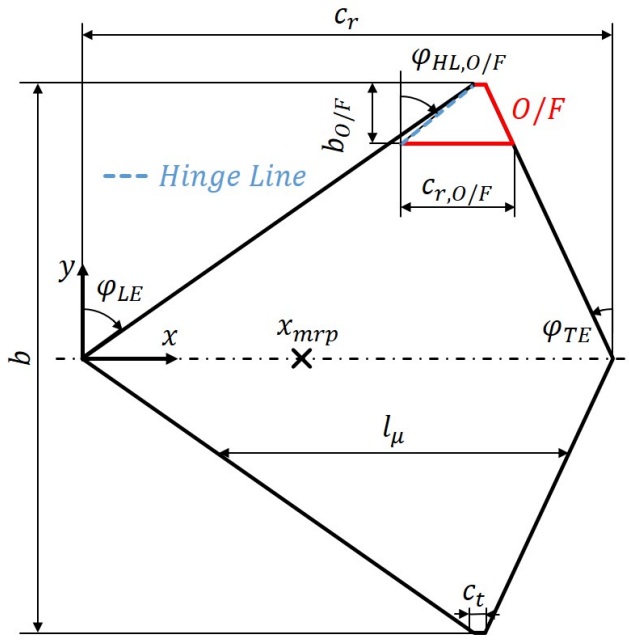

Fig. 1 Diamond wing configuration planform and flap layout.

flap surface, which can be deflected about the hinge line, see Fig. 2. The O/F is completely integrated in the wing, so that the wing shows no discontinuities for the fully retracted flap. In contrast to conventional split flaps, the investigated O/F is deflected about a hinge-line, which is almost parallel to the swept leading edge with a hinge-line angle of $\varphi_{HL,O/F} = 51°$, see Fig. 1. The possible upper and lower O/F surface deflection reads $0 \leq \zeta \leq 50°$. Since only symmetric O/F deflections of the right O/F are considered, the deflection angle is defined as $\zeta = \zeta_R = (\zeta_{R,U} - \zeta_{R,L})/2$. The relative root chord of the O/F reads $\bar{c}_{r,O/F} = c_{r,O/F}/c_r = 0.191$ and the relative O/F area is $\bar{S}_{ref,O/F} = S_{ref,O/F}/S_{ref} = 0.0198$. In lateral direction, the O/F is located in the area of $0.806 \leq \eta \leq 1$ with $\eta = y/(b/2)$, which equals a relative span of the O/F of $\bar{b}_{O/F} = b_{O/F}/(b/2) = 0.194$. Conventional split flaps create the yawing moment by an additional force in x-direction (drag). In contrast, due to the rotation of the hinge line about the z-axis, the O/F creates the yawing moment by an additional force with a x- and y-component, see Fig. 3.

The resulting O/F force vector is rotated about the O/F force vector angle γ_2, which can be calculated as

$$\gamma_2 = arctan\left(\frac{F_{O/F,y}}{F_{O/F,x}}\right). \quad (1)$$

The corresponding lever arm l_γ is defined as

$$l_\gamma = \frac{M_z}{\sqrt{F_{O/F,x}^2 + F_{O/F,y}^2}} \quad (2)$$

and depends on γ_2. This entails two effects. Due to the low aspect ratio of the configuration and the upstream location of the moment reference point in comparison to the O/F, the rotation of the force vector can lead to an increased lever arm l_γ in comparison to a conventional split flap. For an optimized set-up, the optimal lever arm can be $l_{\gamma,opt} = 1.087 \cdot b/2$. Consequently, a higher yawing moment could be achieved with the same force. Furthermore, less drag is necessary for a similar yawing moment, if the moment is created by drag and side force. This would increase the overall efficiency of the aircraft. Another effect, which should increase the effectiveness of the O/F is the formation of a vortex at the O/F back side. The flow separates at the inboard side of the deflected O/F and the shear layer rolls up to a vortex at the back side of the O/F. This vortex would induce a high negative surface pressure at the back side of the flap surface, and thus create a higher yawing moment. The verification of this effect is subject to this analysis.

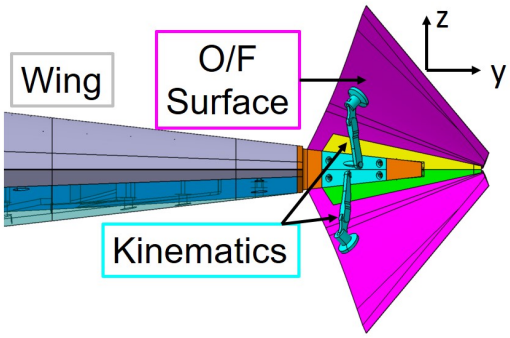

Fig. 2 Back view of the O/F.

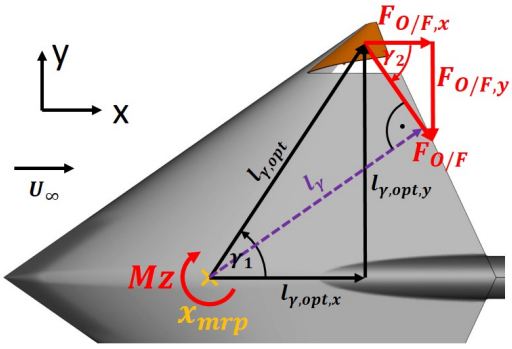

Fig. 3 Sketch of the intended O/F effect.

3 Experimental Approach

3.1 Test Facility and Freestream Conditions

The experimental data is acquired in the wind tunnel A of TUM-AER. It is a Göttingen type low-speed wind tunnel (W/T), with a test section of 1.8 m x 2.4 m x 4.8 m (height x width x length). With an open test section, the maximum velocity is $U_\infty = 65\,m/s$. The W/T model is mounted via a rear sting on a three-axis support, which enables the control of the angle of attack, angle of sideslip, and roll angle. The measurements are performed for a target Mach number of $Ma = 0.13$ and a Reynolds number of $Re = 2.3 \cdot 10^6$ based on the mean aerodynamic chord.

3.2 Wind Tunnel Model

The flying wing configuration described in section 2.1 is manufactured as an aluminum wind tunnel model prepared for a rear sting attachment to a W/T support, see Fig. 4(a). It allows a change of the wing tip section element to replace the clean wing by the O/F. The zero control configuration as well as six different symmetric O/F deflections are realized $\zeta = [0°, 5°, 10°, 20°, 30°, 40°, 50°]$. The model of the O/F also includes fixed rapid prototyping parts representing the flap deflection lever elements for each flap position. The model allows for force and moment as well as steady surface pressure measurements. 192 pressure taps are distributed in 7 chordwise sections $0.1 \leq \frac{x}{c_r} \leq 0.7$ with an increment of $\Delta\frac{x}{c_r} = 0.1$

on the wing upper and lower surface. To ensure a turbulent boundary-layer, trip dots are attached near the wing leading edge. This enables a comparison with fully-turbulent URANS simulations. More detailed information on the application of trip dots on such configurations is given in Ref. [10].

3.3 Measurement Techniques

Two different measurement techniques are applied for this study. The steady forces and moments are measured with an internal six-component strain-gauge balance. The mean values are used for the calculation of the force and moment coefficients.

The flow-field data in the O/F wake is measured in several chord-wise sections by means of stereo particle image velocimetry (Stereo PIV). Figure 4(a) depicts the test set-up for the measurements. The major components of the system are mounted on a three-axis traversing system next to the W/T test section. A double-pulse Nd:Yag laser with an associated wave length of $\Phi = 532\,nm$ and a maximum power of $E = 325\,mJ$ creates the laser beam for the illumination of the measurement plane. The laser beam is converted into a sheet by a laser sheet optic, which is aligned normal to the chord line of the configuration. Two sCMOS cameras are located on each side of the measurement plane. This set-up enables the simultaneous measurement of all three velocity components. Scheimpflugadapter are used in this set-up to account for tilting the sCMOS plane with respect to the off-axis camera [12]. For each measurement plane, 400 sequences are recorded. From this set of recordings, the mean and turbulent velocity flow fields are determined. The measurements are performed in the wake of the left deflected O/F. Since the URANS simulations are performed for the right deflected O/F, the Stereo PIV data is mirrored to the right wing half for the comparison with the numerical results. The defined coordinate system for the Stereo PIV measurement planes has its origin at the trailing edge at the inner interface between O/F and wing, see Fig. 4(b). The origin $\frac{x_w}{c_r} = \frac{y_w}{c_r} = 0$ correlates with the body-fixed coordinates $\frac{x}{c_r} = 0.808$ and $\eta = -0.806$. Eleven cross-flow sections at $0.1 \leq \frac{x_w}{c_r} \leq 0.2$ with an increment of $\Delta\frac{x_w}{c_r} = 0.01$ are measured for every configuration and freestream condition. For the zero angle of attack, an additional section at $\frac{x_w}{c_r} = 0.3$ is measured. The measurements are conducted at three different angles of attack $\alpha = [0°; 10°, 20°]$ and for three O/F deflections $\zeta = [10°; 30°, 50°]$. Only symmetric freestream conditions are considered.

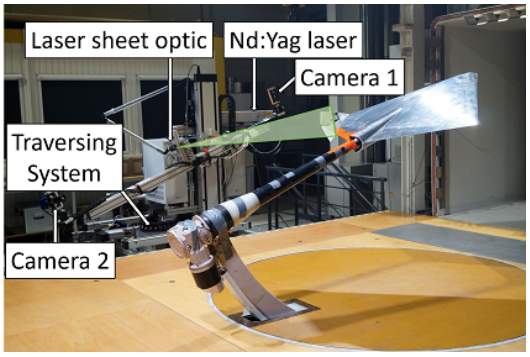

(a) Test set-up.

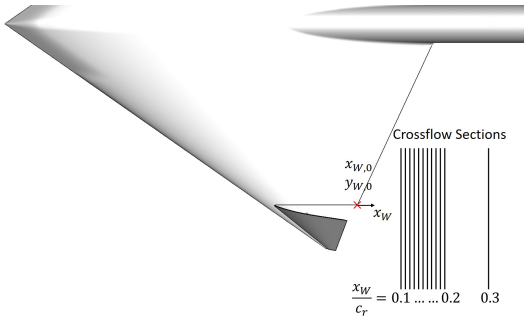

(b) Measurement planes.

Fig. 4 Stereo PIV set-up and measurement planes.

4 Numerical Approach

The numerical simulations are performed with the TAU-Code, which is developed at the German Aerospace Center (DLR) Institute of Aerodynamics and Flow Technology. The TAU-Code is able to solve the three-dimensional compressible (unsteady) Reynolds-Averaged Navier-Stokes ((U)RANS) equations. It is developed for the application of unstructured grids and features

a good parallel efficiency on high-performance computers. The TAU-Code is a collection of different modules responsible for e.g. partitioning, preprocessing, solving, mesh transformation, and mesh adaptation. For the spatial discretization, several upwind and central difference schemes are available. Steady state simulations can be run with a local or global time stepping scheme. A dual time stepping approach is implemented for time-accurate simulations. For turbulent flows, several turbulence models like one and two equation eddy-viscosity models as well as Reynolds stress transport models (RSM) are implemented [13].

4.1 Geometry and Grid Generation

For the numerical investigations, the same geometry as for the experiments is used. The support of the W/T set-up is modeled by an extension of the rear sting up to one root chord length downstream of the root-chord trailing edge. The W/T test section is not considered in the computational analysis. The numerical grid is created with the unstructured hybrid grid generation software CENTAUR [1]. Due to the asymmetric geometry, the full model needs to be simulated. To minimize the asymmetries in the grid, a modular meshing approach is applied. The O/F is located in an interface box. This enables the exchange of the geometry and recreation of the numerical grid inside the box, without changing the overall mesh. The applied grids for this study are based on former investigations, which included a grid independence and a y^+-analysis [10]. The numerical grid is significantly refined in the vicinity of the wing leading and trailing edge, in the vicinity and in the wake of the O/F, and above the upper wing side, see Fig. 5. Detailed information on the zero control configuration grid and the grids for the deflected O/F is given in [10] and [9], respectively.

[1]Data available online at https://www.centaursoft.com [retrieved June 2018].

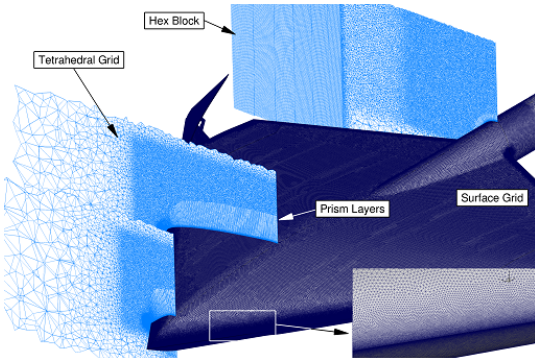

Fig. 5 Numerical Grid of the configuration with deflected O/F.

4.2 Applied Numerical Set-Up

The numerical simulations are performed at freestream conditions similar to the experiments with a Reynolds number of $Re = 2.3 \cdot 10^6$, a Mach number of $Ma = 0.13$ and a freestream velocity of $U_\infty = 44.23\,m/s$. For the spatial discretization, a second-order central scheme introduced by Jameson [14] is applied. The required artificial viscosity is given by a matrix-dissipation scheme, which leads to a more upwind biased method [15]. For the time discretization, an implicit Backward-Euler scheme with a LUSGS algorithm is chosen. A 3W multigrid cycle is applied to speed up the convergence of the solution. For the time-accurate simulations, a characteristic time step of $\Delta t^* = \frac{\Delta t \cdot U_\infty}{l_\mu} \approx 0.02$ is chosen in accordance with Ref. [16]. This leads to a physical time step of $\Delta t = 4 \cdot 10^{-4}\,s$. All simulations are run fully-turbulent and with the Spalart-Allmaras turbulence model [17] in the SA-neg version [18]. This turbulence model showed good results in former investigations on low-aspect-ratio wing configurations with round leading edges [9, 10].

5 Results

In this section, the effect of the deflected O/F on the forces and moments and the flow around the wing is discussed. The evolving forces and moments originating from the deflected O/F are discussed by means of aerodynamic coefficient in-

crements

$$\Delta C_i = C_i(\zeta) - C_i(\zeta = 0^\circ), \tag{3}$$

the O/F force vector angle γ_2 and the relative lever arm l_γ/s, see Fig. 3. Assuming, that the incremental forces determined from the global aerodynamic coefficients are only originating from the O/F, they represent the O/F forces. The O/F forces can also be given as non-dimensional coefficients

$$C_{O/F,i} = \frac{F_{O/F,i}}{q \cdot A_{ref}} \tag{4}$$

For symmetric freestream conditions, the O/F forces can then be expressed as

$$C_{O/F,x} = \Delta C_D \cos\alpha - \Delta C_L \sin\alpha, \tag{5}$$

$$C_{O/F,y} = \Delta C_Y. \tag{6}$$

In the following Sections 5.1-5.3, all analyses are discussed for a freestream condition of $\alpha = \beta = 0^\circ$.

5.1 Force and Moment Characteristics

For a zero degree angle of attack, the measured global aerodynamic coefficient increments can be seen as the force increments originating only from the deflected O/F and consequently as the O/F forces. As it is described in Ref. [9], the SA-neg model acts well in predicting the flow around the overall configuration without deflected O/F, but shows deficits for large O/F deflections. The zero degree angle of attack case allows a detailed discussion of the O/F characteristics without influence of the upstream flow due to vortex flow or separated flow with flow reversal. Thus, an evaluation of the SA-neg model in predicting the flow around the deflected O/F is possible. Figure 6 shows the drag, side force and yawing moment coefficient increment as well as the O/F force vector angle γ_2 and the relative lever arm l_γ/s versus the O/F deflection ζ for the W/T data and the SA-neg URANS results. The drag and side force coefficient increment both show a non-linear characteristic with respect to ζ, see Figs. 6(a) and 6(b). The comparable magnitude of both coefficients also indicates the effect of a rotated O/F force vector. The originating yawing moment is created by an increase in drag and side force. This non-linearity is also represented by the yawing moment coefficient increment, which shows an increasing effectiveness of the O/F with increasing deflection, see Fig. 6(c). The O/F force vector angle γ_2 confirms the intended effect of the O/F with a significant rotation of the force vector of almost 50 degree for a maximum O/F deflection. This effect is diminished for small O/F deflections, whereas a minimum of $\gamma_2 = 20^\circ$ still represents a considerable rotation of the force vector. Fig. 6(e) describes the relative lever arm versus the O/F deflection. It can be observed, that the relative lever arm is bigger than 0.8 for $\zeta \geq 10^\circ$. The lever arm slightly increases with higher O/F deflection up to a value of almost 1. This matches with the O/F force vector angle characteristic. Due to an increasing contribution of the side force, the vector is rotated about γ_2 and the lever arm is increased.

The URANS simulations with the SA-neg turbulence model show a good agreement and a comparable characteristic with the experimental data. Considering the drag and side force coefficient increment, the numerical results predict a similar trend with respect to ζ. For a small to moderate O/F deflection, the values show a good agreement. At $\zeta = 50^\circ$, however, the URANS computations do not predict the reduction of the forces as it is the case for the experiments. Overall, the disagreements in the drag and side force coefficient increment are small, whereas the URANS simulation slightly over predicts both values in magnitude. This results in a relatively higher deviation in the yawing moment coefficient increment. The O/F force vector angle and the relative lever arm are represented well by the numerical results. The characteristic with respect to ζ as well as the absolute values are similar. This indicates, that the resulting O/F force vector has the same direction in both numerical simulation and W/T. Consequently, the disagreement in the yawing moment coefficient increment, especially at $\zeta = 50^\circ$, originates from a different absolute value of the O/F force vector. Accord-

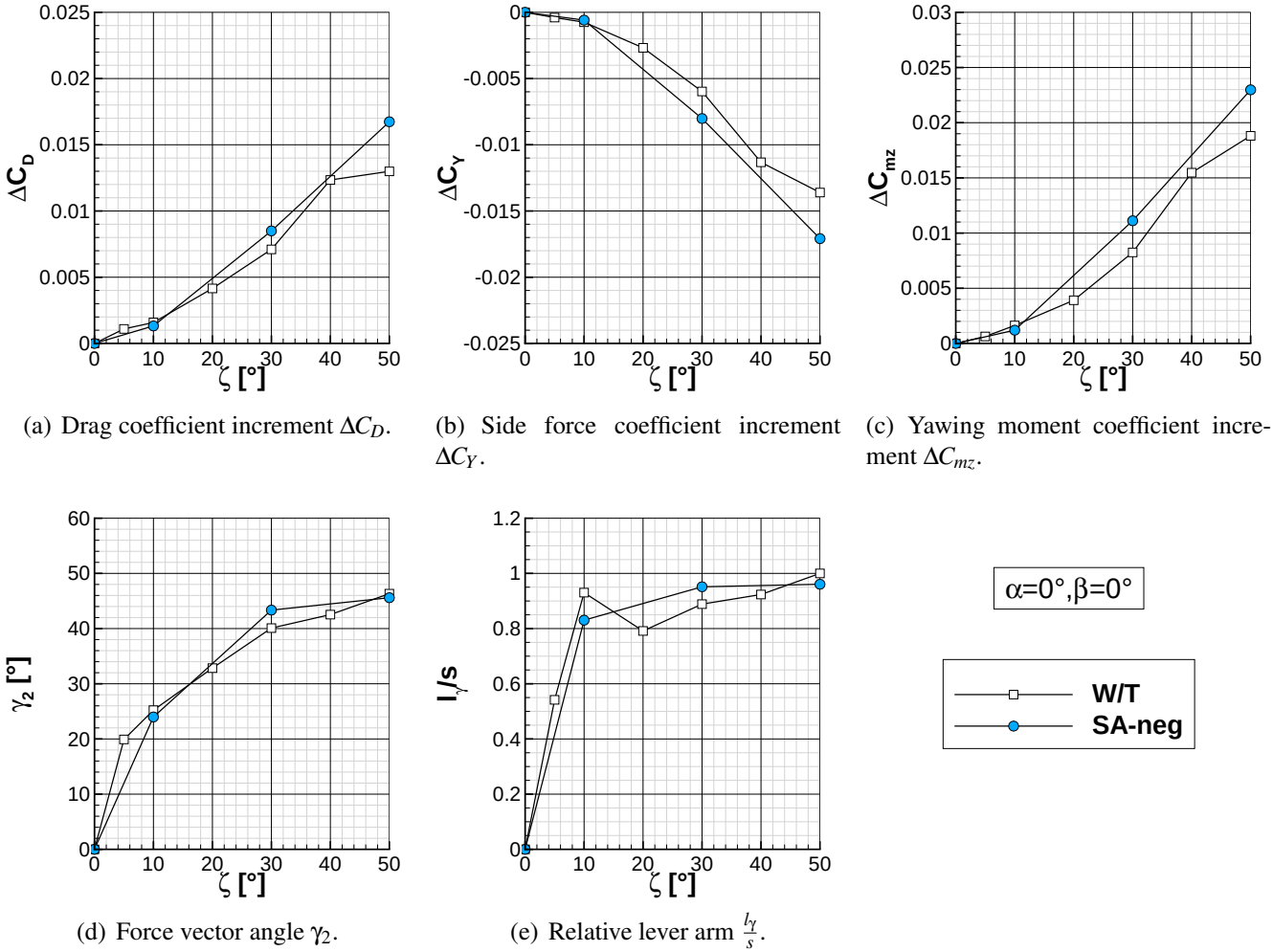

(a) Drag coefficient increment ΔC_D.

(b) Side force coefficient increment ΔC_Y.

(c) Yawing moment coefficient increment ΔC_{mz}.

(d) Force vector angle γ_2.

(e) Relative lever arm $\frac{l_y}{s}$.

Fig. 6 Force and moment coefficient increments and O/F force vector information versus O/F deflection at $\alpha = 0°$ and $\beta = 0°$.

ing to the URANS results, the major contribution of more than 80 % to the yawing-moment increment originates from the back side of the O/F surfaces due to a reduced surface pressure at this side. At the O/F surface front side, the surface pressure only slightly increases with the O/F deflection and thus hardly contributes to the yawing moment.

5.2 Wake Flow Characteristics

A detailed analysis of the O/F flow is possible by means of the flow field data obtained in the wake of the O/F with Stereo PIV measurements. The occurring aerodynamic coefficient increments are associated with the wake flow of the O/F. The non-dimensional axial and lateral velocity u/U_∞ and v/U_∞, respectively, are discussed to highlight the changes in the velocity fields corresponding to the aerodynamic force increments.

The positive drag increment created by the deflected O/F is represented by a reduced axial velocity, see Fig. 7. The illustrations show u/U_∞ in the $\frac{x_w}{c_r} = 0.10$ section for the three different O/F deflections including the W/T data and the URANS SA-neg results. The two black, vertical lines in each plot indicate the inner and outer span-wise border of the O/F. In the inboard area at $y/s < 0.8$, the thin layer of reduced velocity of $u/U_\infty \approx 0.7$ indicates the shear layer shed at the trailing edge. For a small O/F deflection of $\zeta = 10°$, only a small additional area exhibits a velocity deficit with minimal reduced axial ve-

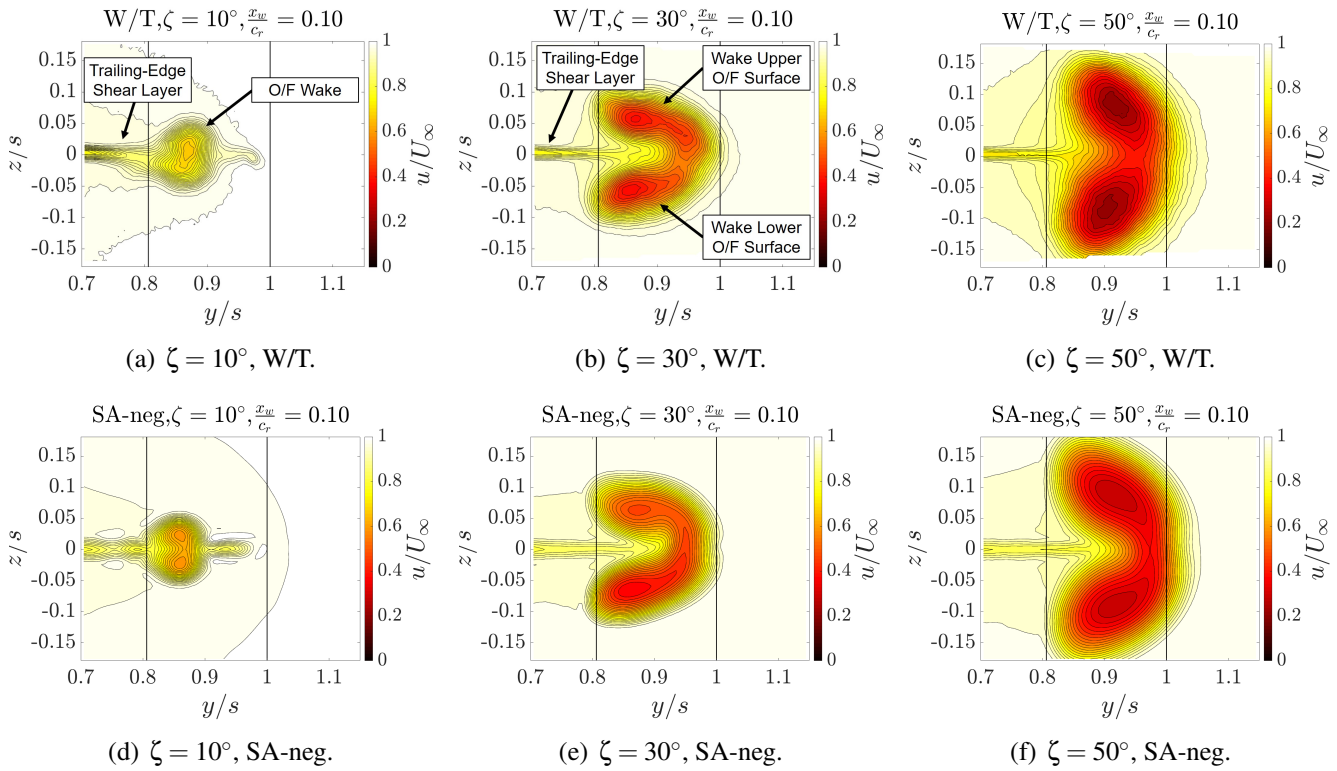

(a) $\zeta = 10°$, W/T. (b) $\zeta = 30°$, W/T. (c) $\zeta = 50°$, W/T.

(d) $\zeta = 10°$, SA-neg. (e) $\zeta = 30°$, SA-neg. (f) $\zeta = 50°$, SA-neg.

Fig. 7 Non-dimensional axial velocity u/U_∞ at $\alpha = 0°$, $\beta = 0°$ and $x/c_r = 0.10$ for different O/F deflection angles obtained from numerical and experimental data.

locities of $u/U_\infty \approx 0.6$, see Fig. 7(a). This corresponds to the small drag coefficient increment for this configuration. The area of reduced axial velocity is also restricted to the inboard section of the O/F of $0.8 < y/s < 0.9$, which is due to the deflection of the O/F about the rotated hinge line. An increased O/F deflection of 30 degree significantly increases the span-wise area of reduced axial velocity, the vertical area, and the absolute value of the velocity reduction. A further increase of the O/F deflection only affects the vertical area and the absolute value. The restricted span-wise area of the O/F affecting the flow, is probably the reason for the strong nonlinear characteristics and the low effectiveness at small O/F deflection angles. The area affected by the O/F increases in positive span-wise direction up to $y/s \approx 1.05$ for $\zeta = 50°$. The velocity reduction is most significant directly behind the deflected upper and lower O/F surface, c.f. Fig. 2, with velocity levels of $u/U_\infty \approx 0.2 - 0.4$ for $\zeta \geq 30°$, see Fig. 7(b) and 7(c). In between the deflected O/F surfaces, the velocity level is similar to the one, observed at the trailing-edge shear layer. Comparing the URANS SA-neg results with the W/T data, reveals a good representation of the flow structures in the wake by the numerical simulations, see Figs. 7(a)-7(c) and Figs. 7(d)-7(f). The structure of the velocity deficit as well as the velocity levels are comparable. For $\zeta = 50°$, the area of reduced velocity is predicted slightly larger by the numerical simulation, and the maximum reduction in the wake of the upper and lower O/F surface is smaller in comparison with the experimental data.

The non-dimensional lateral velocity in the wake of the O/F is illustrated in Fig. 8. The same configurations, data sources, freestream conditions and sections are shown as in Fig. 7. For the small O/F deflection of ten degree, slightly increased velocities can be observed between the deflected O/F surfaces at $y/s \approx 0.83$, see Fig. 8(a). The small lateral velocities, as well as the mixture of positive and negative lateral veloc-

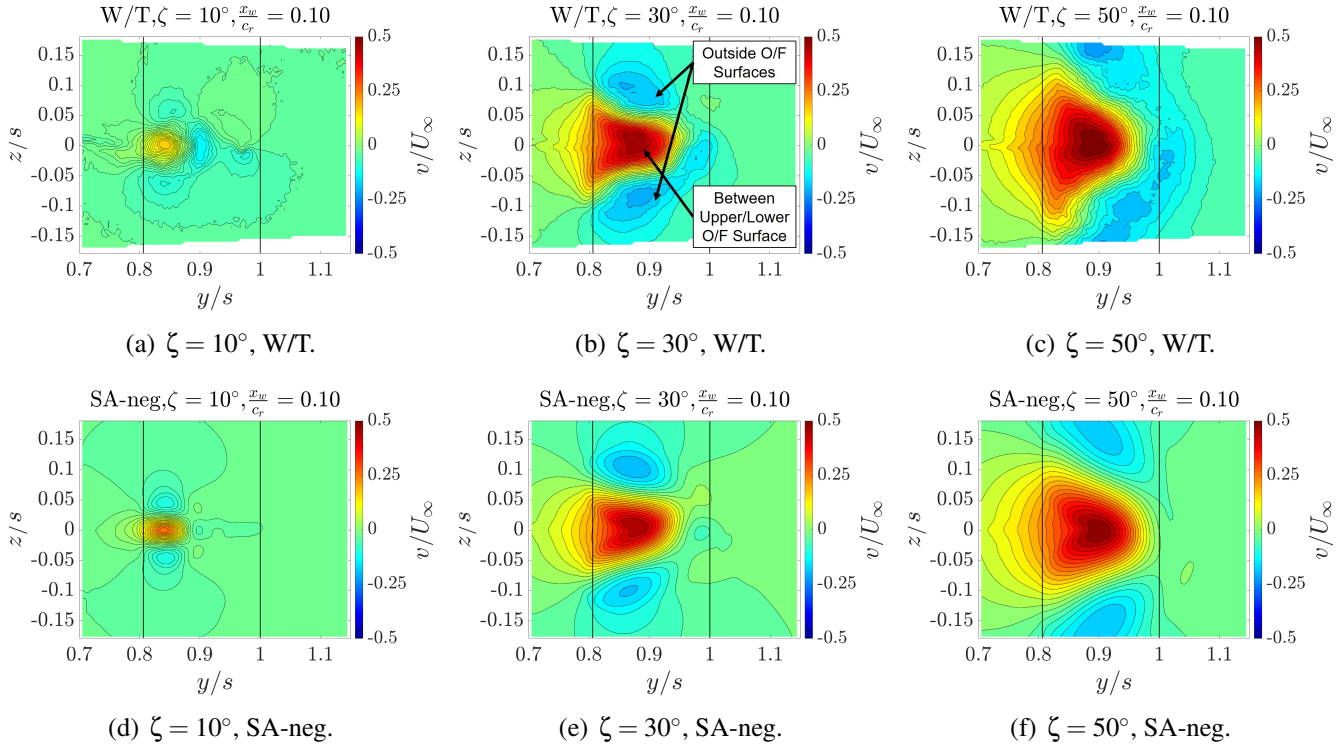

(a) $\zeta = 10°$, W/T. (b) $\zeta = 30°$, W/T. (c) $\zeta = 50°$, W/T.

(d) $\zeta = 10°$, SA-neg. (e) $\zeta = 30°$, SA-neg. (f) $\zeta = 50°$, SA-neg.

Fig. 8 Non-dimensional lateral velocity v/U_∞ at $\alpha = 0°$, $\beta = 0°$ and $x/c_r = 0.10$ for different O/F deflection angles obtained from numerical and experimental data.

ities correspond to the small side force coefficient increment. In accordance with the axial velocity deficit, the effect of the 10 degree deflected O/F on the lateral velocity is restricted to a small span-wise area. Considerably higher lateral velocities are observed for $\zeta = 30°$, see Fig. 8(b). Between the deflected O/F surfaces, significant positive values of $v/U_\infty \approx 0.4$ are observed. The span-wise area affected by the flow deflection in the wing outboard direction is significantly extended in comparison to the smaller O/F deflection. Above and below the upper and lower O/F surface, respectively, as well as in the wing tip area at $y/s \approx 1$, slightly negative lateral velocities are present. A further increase of ζ does not change the characteristic itself, but the affected area and the intensities of the induced velocities, see Fig. 8(c). Both, the affected area and the intensities increase with the O/F deflection. A comparison of the W/T data with the URANS results shows a satisfying agreement, see Figs. 8(a)-8(c) and Figs. 8(d)-8(f). The characteristic distribution of the lateral velocity is met well by the numerical simulations. The trends with an extension of the affected area of induced lateral velocities and increasing velocity levels with ζ are predicted by the numerical simulation. For $\zeta = 10°$, the positive and negative velocity levels are slightly over predicted by the URANS simulation. At higher O/F deflections, the biggest discrepancy is observed in the outboard section at $y/s \approx 1$. In this area, the URANS simulations do not predict the negative lateral velocities, which are observed in the experiments. This effect is most significant at $\zeta = 50°$.

Next, the span-wise distribution of the axial velocity and the lateral velocity in the wake of the O/F is discussed. The integral in vertical direction of the axial velocity deficit $\int (1 - u/U_\infty)\, dz$ and the lateral velocity $\int v/U_\infty dz$ is shown versus y/s for all O/F deflections at $x_w/c_r = 0.10$ for both data sources, see Fig. 9. The integrals are divided by l_μ to get non-dimensional values. This data gives a more quantitative and detailed information on the induced velocities per wing span. Furthermore, it enables a more quantitative

comparison of the numerical results with the experimental data.

Figure 9(a) illustrates the span-wise distribution of the integral of the velocity deficit. Outboard of the O/F at $y/s > 1.1$, the value converges to zero for all O/F deflections and data sources, since no influence of the body on the flow is present. Inboard of the O/F, the effect of the trailing-edge shear layer is visible by slightly increased values above zero. The ten-degree deflected O/F, represented by the dotted lines, leads to a slightly increased velocity deficit at $0.8 < y/s < 0.9$. With increasing O/F deflection, the values significantly increase. Furthermore, the span-wise location of the maximum moves further outboard and the overall affected span-wise are is extended. The span-wise barycenter of the velocity deficit for the different O/F deflections and data sources is given in Tab. 1. The barycenter moves from $y/s = 0.83$ for the 10 degree deflected O/F to $y/s = 0.91$ for the 50 degree deflected O/F. For $\zeta \leq 30°$, the URANS simulations predict the span-wise characteristic of the velocity deficit very well. In some areas, the numerical simulation predicts a slightly too high velocity deficit in comparison with the W/T results. The characteristic of the maximum O/F deflection is not fully reliable in the area of $y/s \approx 0.9$, because the affected area by the O/F is not completely captured in the frame. Consequently, the correct maximum values might be a little bit higher. However, in- and outboard, a comparison between the numerical simulation and W/T data is valid. In the W/T data, the affected area in the inboard and outboard section of the O/F is slightly larger than in the URANS result. The span-wise barycenter of the velocity deficit is also predicted well by numerical simulations, see Tab. 1.

Figure 9(b) shows the integral in z-direction of the lateral velocity component. This gives an indication on the overall induced lateral velocity per span-wise section of the O/F. Similar to the axial velocity deficit, the overall induced lateral velocity component per section strongly increases with increasing deflection. For the ten degree deflected O/F, almost no lateral velocity

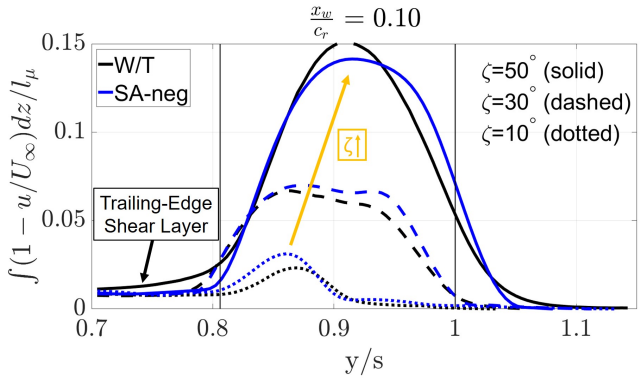

(a) Non-dimensional integral of $1-u/U_\infty$ in z-direction.

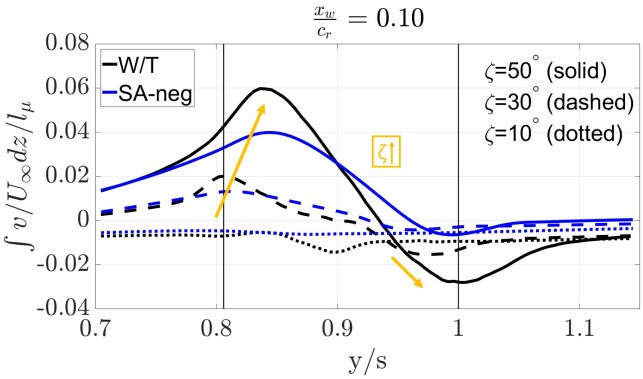

(b) Non-dimensional integral of v/U_∞ in z-direction.

Fig. 9 Non-dimensional integral in z-direction of the velocity deficit $1-u/U_\infty$ and the lateral velocity v/U_∞ versus y/s at $x_w/c_r = 0.10$ at $\alpha = 0°$ and $\beta = 0°$ for all O/F deflections and data sources.

per span-wise section is present. The positive and negative lateral velocities almost cancel each other out in the span-wise sections. The W/T data shows a slight reduction at $y/s \approx 0.9$, which is not observed in the URANS results. With increasing O/F deflection, positive values are observed in the inboard section, and negative values are present in the outboard section of the O/F.

Table 1 Lateral barycenter of the velocity deficit at $\alpha = 0°$ and $\beta = 0°$ for the different O/F deflections and data sources.

ζ [deg]	W/T [y/s]	SA-neg [y/s]
10	0.83	0.84
30	0.88	0.89
50	0.91	0.91

Consequently, the positive lateral velocities in the area between the deflected O/F surfaces outweighs the negative velocities outside of the O/F surfaces. In the outboard section at $y/s > 0.95$, it is the other way around. The peaks of the integral values increase and move further outboard with the O/F deflection. Overall, the affected area in inboard direction is significantly larger in case of the lateral velocity integral in comparison to the axial velocity deficit integral. A comparison between the URANS results and experiment reveals a larger deviation in the outboard section of the O/F. The integral values are higher for the numerical simulations, which corresponds to the absent negative lateral velocities in the outboard section in the numerical results, compare Fig. 8(f). The large deviation for the 50 degree deflected O/F at $y/s \approx 0.85$ is motivated by the too small frame measured in the Stereo PIV tests. In the outboard section at $y/s \approx 1$, the wrong prediction of the lateral velocity by the numerical simulation is the reason for the deviation.

Both, the integral values of the axial velocity deficit and the lateral velocity indicate a significantly increasing influence with ζ and an outboard movement of the maximum values. This corresponds with the deflection of the O/F around the rotated hing line, which moves the center of the O/F surfaces more outboard. The characteristics of the wake flow correspond to the force and moment characteristics. Although some small disagreements are observed in the yawing moment coefficient increment between the experimental and the numerical data, the applied numerical set-up represents the wake flow characteristics very well with minor deviations to the experimental data. Therefore, the URANS simulations are seen to be reliable for the investigated cases.

5.3 Flow Characteristics at the Outboard Split Flap

Figure 10 illustrates the front and backside of the 30 degree deflected O/F. Figure 10(a) shows the surface pressure coefficient c_p and the skin-friction lines obtained from the URANS SA-neg simulation. As it was already mentioned, the surface pressure level at the O/F front side is hardly increased. At the inboard section of the O/F front side, the flow is deflected in inboard direction towards the side edge of the O/F. In the front part of the O/F, the shear layer is then deflected in outboard direction and rolls up to a vortex (O/F Vortex). The flow at the wing in the area inboard of the O/F is deflected and accelerated in outboard direction into the area between the two deflected O/F surfaces. The flow is accelerated in this direction due to the decreased pressure be-

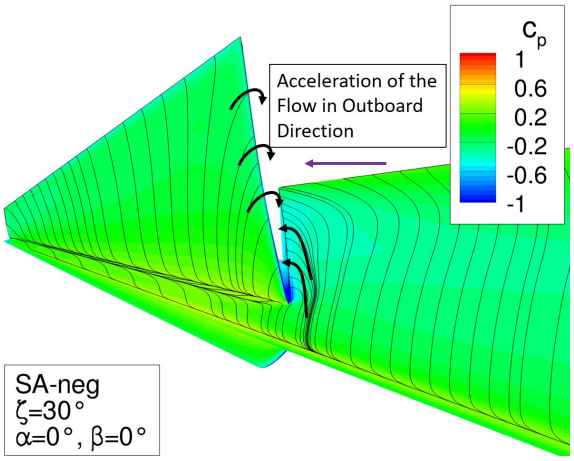

(a) Front view of the O/F with the surface pressure coefficient c_p and the skin-friction lines.

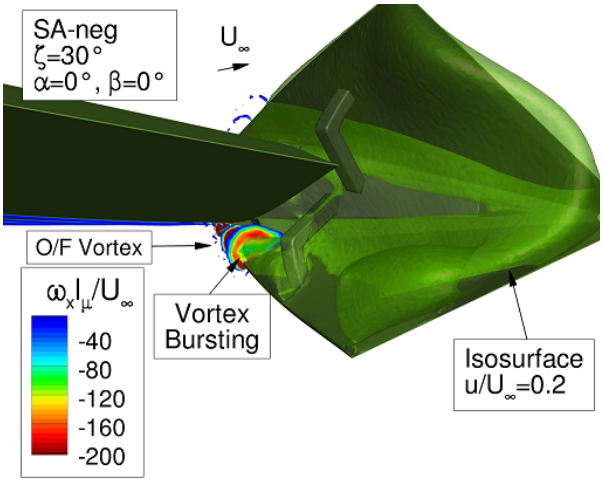

(b) Back view with non-dimensional axial vorticity slices and an iso surface of $u/U_\infty = 0.2$.

Fig. 10 Surface and flow field data for $\zeta = 30°$ at $\alpha = 0°$ and $\beta = 0°$ obtained from the URANS SA-neg computations.

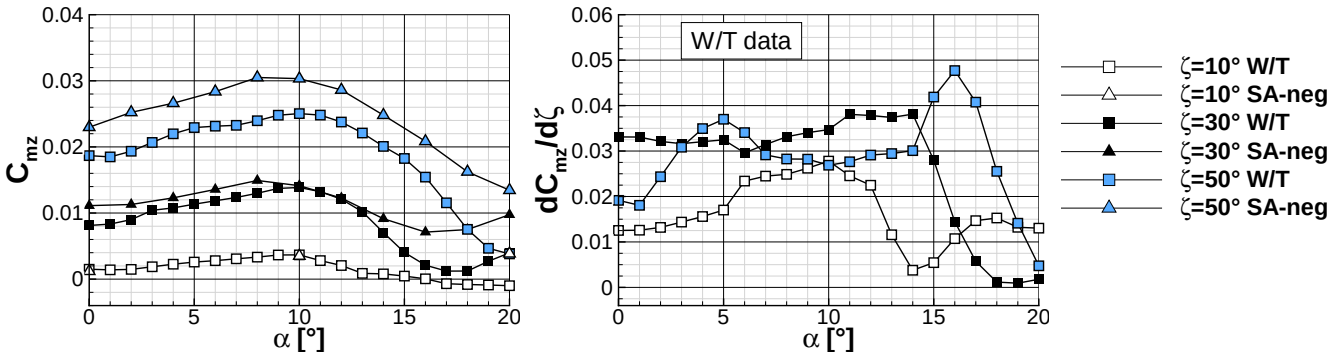

(a) Yawing moment coefficient C_{mz}. (b) O/F efficiency factor $dC_{mz}/d\zeta$.

Fig. 11 Yaw control effectiveness and efficiency for the 10, 30 and 50 degree deflected O/F obtained from experimental and numerical data versus α at $\beta = 0°$.

hind the deflected O/F. This is also seen by the reduced surface pressure at the outboard section of the wing. Figure 11(c) depicts the back side of the O/F. At the lower O/F surface, the non-dimensional axial vorticity $\omega_x \cdot l_\mu / U_\infty$ indicates the presence of the O/F vortex. Under the vortex axis, significantly reduced pressure levels are present at the O/F surface. However, the vortex immediately bursts due to the adverse pressure gradient evolved by the downstream located flap lever arm element. The vortex bursting is indicated by the iso-surface of the axial velocity distribution $u/U_\infty = 0.2$. Therefore, the effect of the vortex on the overall yawing moment is minor. Furthermore, the O/F vortex is not observed for the ten and fifty degree deflected O/F. The iso-surface of the axial velocity indicates the areas of reduced axial velocity in the vicinity of the inner side of the O/F surfaces and in the outboard section of the O/F. This structure is represented by the axial velocity in the O/F wake, see Fig. 7.

5.4 Overall Flap Effectiveness and Efficiency

Subsequent to the detailed investigation of the O/F characteristics and the wake flow, the overall characteristics concerning the yaw control effectiveness and efficiency are considered. The yaw-control effectiveness is discussed by means of the yawing moment coefficient C_{mz} and the yaw-control efficiency by means of the O/F efficiency factor $dC_{mz}/d\zeta$. The derivative is determined by a linear interpolation around the discrete data points. Since only a small number of O/F deflection angles is simulated ($\zeta = [0°, 10°, 30°, 50°]$) with URANS, the O/F efficiency factor is exclusively calculated for the experimental data. It is available for $\zeta = [0°, 5°, 10°, 20°, 30°, 40°, 50°]$, which results in more precise values for the derivative. A positive yawing moment coefficient and O/F efficiency factor represent the desired characteristic for the right O/F deflected. A more detailed analysis on the yaw control efficiency and effectiveness is also given in [9].

Figure 11(a) illustrates the yawing-moment coefficient versus α at $\beta = 0°$ for both data sources. In general, the same characteristics with respect to α are observed for all O/F deflections. The yaw control effectiveness increases up to $\alpha = 10°$, where a local maximum is reached. For a further increasing angle of attack, the yaw control effectiveness steadily decreases. This effect strengthens with increasing O/F deflection. The maximum achievable yawing moment coefficient reads $C_{mz} = 0.025$ at $\alpha = 10°$ for the 50 degree deflected O/F. The achievable yawing moment significantly decreases for small O/F deflections. The ten degree deflected O/F hardly exhibits an effect on the yawing moment. The URANS simulations predict well the general characteristics. However, the reduction in the effectiveness at high angles of attack is less pronounced and the absolute values show some disagreements espe-

cially for $\zeta = 50°$. The deviation between the experiments and the numerical simulations in the small angle of attack range has been analyzed in Secs. 5.1 and 5.2.

The yaw control efficiency is shown in Fig. 11(b). A positive O/F efficiency factor is observed throughout the whole angle-of-attack polar for all ζ. Consequently, an increase in the O/F deflection always results in a higher yawing moment coefficient. Strong non-linear characteristics with respect to α and ζ are indicated for all flap deflections, not showing a clear trend. However, at higher angles of attack, the efficiency significantly decreases and almost reaches a value of zero for all ζ. A satisfying efficiency is provided up to $\alpha \approx 15°$. The maximum achievable O/F efficiency factor for the considered configurations and freestream conditions reads $dC_{mz}/d\zeta = 0.048$ at $\alpha = 16°$ for $\zeta = 30°$.

6 Conclusion and Outlook

The aerodynamics of a novel yaw-control device for a low-aspect-ratio flying-wing configuration has been presented. Experimental data has been used to determine the characteristics of the O/F at low-speed W/T conditions. Forces and moments as well as flow field measurements in the wake of the deflected O/F have been performed to obtain an experimental data base. Furthermore, URANS simulations have been conducted at similar conditions, to evaluate the capabilities of the numerical method to predict the flow around the deflected O/F. The novel layout of the O/F with its hinge line along the 55 degree swept leading edge, is designed to utilize several effects to obtain a more effective yaw-control device. The yawing moment is created by an increased drag and side force at the deflected O/F. This effect strengthens with increasing O/F deflection. The force vector consisting of a x- and y-component in combination with an axial distance between the moment reference point and the point of load incidence at the O/F results in a slightly increased lever arm in comparison to conventional split flaps. Furthermore, less drag is required for a similar yawing moment. However, optimizing the hinge-line alignment and/or the O/F layout could further increase the effectiveness of the O/F. Significant axial and lateral velocities are introduced by the O/F deflection. The strong non-linear characteristics at small O/F deflections can be associated with the reduced span-wise sphere of action at small O/F deflections. The URANS results represent the forces and moments as well as the wake flow characteristics well. The disagreements in the yawing moment coefficient between the numerical simulations and experiment are a combination of small deviations in the drag and side force increment at the O/F. The characteristics with respect to the O/F deflection angle are met very well. The flow structures in the wake of the O/F are predicted in a satisfactory way by the numerical simulations, with minor disagreements in the absolute values and the size of the structure. Overall, the CFD method is seen to be appropriate for the applied configuration. Further, the O/F characteristics at higher angles of attack will be looked at, since a significant reduction of the O/F effectiveness has been observed for $\alpha > 10°$.

7 Contact Author Email Address

mailto: stefan.pfnuer@tum.de

Acknowledgments

The support of this investigation by Airbus Defence and Space within the VitAM/VitAMInABC (Virtual Aircraft Model for the Industrial Assessment of Blended Wing Body Controllability, FKZ: 20A1504C) project is gratefully acknowledged. Furthermore, the authors thank the German Aerospace Center (DLR) for providing the DLR TAU-Code used for the numerical investigations. Moreover, the authors gratefully acknowledge the Gauss Centre for Supercomputing e.V. (www.gauss-centre.eu) for funding this project by providing computing time on the GCS Supercomputer SuperMUC at Leibniz Supercomputing Centre (LRZ, www.lrz.de). The support of our colleague Florian Knoth during the Stereo PIV measurements is also highly appreciated.

References

[1] J. P. Campbell and C. L. Seacord. Determination of the Stability and Control Characteristics of a Tailless All-Wing Airplane Model With Sweepback in the Langley Free-Flight Tunnel, NACA-ACR-L5A13, 1945.

[2] K. Crenshaw and B. Flanagan. Testing the Flying Wing. 33rd Joint Propulsion Conference & Exhibit, Seattle (WA), AIAA Paper 1997-3262, 1997.

[3] C. J. Donlan. An Interim Report on the Stability and Control of Tailless Airplanes, NACA/TR-796, 1994.

[4] A. R. Weyl. Tailless Aircraft and Flying Wings: A Study of Evolution and Their Problems. *Aircr. Eng. Aerosp. Technol.*, 17(2):41–46, 1945.

[5] W. J. Gillard and K. M. Dorsett. Directional Control for Tailless Aircraft Using All Moving Wing Tips. 22nd Atmospheric Flight Mechanics Conference, New Orleans (LA), AIAA Paper 1997-3487, 1997.

[6] P. Bourding, A. Gatto, and M. I. Friswell. Potential of Articulated Split Wingtips for Morphing-Based Control of a Flying Wing. 25th Applied Aerodynamics Conference, Miami (FL), AIAA Paper 2007-4443, 2007.

[7] J. L. Fulker and J. E. Alderman. Three-dimensional Compliant Flows for Lateral Control Applications. 43rd Aerospace Science Meeting & Exhibit, Reno (NV), AIAA Paper 2005-0240, 2005.

[8] W. Sears. Flying-Wing Airplanes: The XB-35/YB-49 Programm. The Evolution of Aircraft Wing Design, Proceedings of the Symposium, Dayton (OH), AIAA Paper 1980-3036, 1980.

[9] S. Pfnür, S. Oppelt, and C. Breitsamter. Yaw-Control Efficiency Analysis for a Diamond Wing Configuration. 66th Deutscher Luft- und Raumfahrtkongress, Munich, Germany, DLRK 2017-0020, 2017.

[10] A. Hövelmann. *Analysis and Control of Partly-Developed Leading-Edge Vortices*. Dissertation, Technische Universität München. Dr. Hut Verlag, ISBN 978-3-8439-2807-6, 2016.

[11] A. Hövelmann and C. Breitsamter. Leading-Edge Geometry Effects on the Vortex Formation of a Diamond-Wing Configuration. *J. Aircr.*, 52(2):1596–1610, 2015.

[12] M. Raffel, C. E. Willert, S. T. Wereley, and J. Kompenhans. *Particle Image Velocimetry - A Practical Guide*. 2nd Edition. Springer Verlag, ISBN 978-3-540-72307-3, 2007.

[13] T. Gerhold. Overview of the Hybrid RANS Code TAU. In *MEGAFLOW-Numerical Flow Simulation for Aircraft Design, Vol. 89 of Notes on Numerical Fluid Mechanics and Multidisciplinary Design, Springer Verlag, 2005*.

[14] A. Jameson, W. Schmidt, and E. Turkel. Numerical Solutions of the Euler Equations by Finite Volume Methods Using Runge-Kutta Time Stepping Schemes. 14th AIAA Fluid and Plasma Dynamics Conference, Palo Alto (CA), AIAA Paper 1981-1259, 1981.

[15] E. Turkel. Improving the Accuracy of Central Difference Schemes, NASA-CR-181712, 1988.

[16] N. T. Frink, M. Tomac, and A. Rizzi. Collaborative Study of Incipient Separation on 53deg-Swept Diamond Wing. *Aerosp. Sci. Technol.*, 57(1):76–89, 2016.

[17] P. R. Spalart and S. R. Allmaras. A One-Equation Turbulence Model for Aerodynamic Flows. 30rd Aerospace Sciences Meeting & Exhibit, Reno (NV), AIAA Paper 1992-0439, 1992.

[18] S. R. Allmaras, F. T. Johnson, and P. R. Spalart. Modifications and Clarifications for the Implementation of the Spalart-Allmaras Turbulence Model. 7th International Conference on Computational Fluid Dynamics, Big Island (HI), United States, ICCFD7-1902, 2012.

Copyright Statement